SCIENCE CHINA
Technological Sciences

Special Issue: Celebrating the 70th Anniversary of School of Mechanical Science and Engineering of HUST
• Article •

September 2022 Vol. 65 No. 9: 2143–2155
https://doi.org/10.1007/s11431-022-2082-4

Real-time adaptive particle image velocimetry for accurate unsteady flow field measurements

OUYANG ZhenXing, YANG Hua*, LU Jin, HUANG YongAn & YIN ZhouPing

State Key Laboratory of Digital Manufacturing Equipment and Technology, School of Mechanical Science and Engineering, Huazhong University of Science and Technology, Wuhan 430074, China

Received April 5, 2022; accepted May 18, 2022; published online August 15, 2022

Almost all conventional open-loop particle image velocimetry (PIV) methods employ fixed-interval-time optical imaging technology and the time-consuming cross-correlation-based PIV measurement algorithm to calculate the velocity field. In this study, a novel real-time adaptive particle image velocity (RTA-PIV) method is proposed to accurately measure the instantaneous velocity field of an unsteady flow field. In the proposed closed-loop RTA-PIV method, a new correlation-filter-based PIV measurement algorithm is introduced to calculate the velocity field in real time. Then, a Kalman predictor model is established to predict the velocity of the next time instant and a suitable interval time can be determined. To adaptively adjust the interval time for capturing two particle images, a new high-speed frame-straddling vision system is developed for the proposed RTA-PIV method. To fully analyze the performance of the RTA-PIV method, we conducted a series of numerical experiments on ground-truth image pairs and on real-world image sequences.

real-time adaptive particle image velocimetry, flow field measurement, high-speed vision, correlation filter

Citation: Ouyang Z X, Yang H, Lu J, et al. Real-time adaptive particle image velocimetry for accurate unsteady flow field measurements. Sci China Tech Sci, 2022, 65: 2143–2155, https://doi.org/10.1007/s11431-022-2082-4

1 Introduction

In the field of experimental fluid mechanics, particle image velocimetry (PIV) is a well-known non-contact measurement methodology for accurately estimating the velocity fields of fluid flows, which provides intuitional flow field information for analyzing the complex flow mechanisms [1]. In general, the conventional PIV method is an open-loop measurement method, and it consists of the following four steps [2, 3]. First, many tracer particles with small quality and size are seeded into the fluid flow to follow its movement. Subsequently, a sheet of pulsed laser light is employed to highly illuminate these tracer particles undergoing short displacements with a fixed interval time. Meanwhile, a double frame-straddling vision camera is utilized to synchronously capture two digital images of the tracer particles. Finally, a PIV measurement algorithm is applied to these two digital images to accurately estimate the instantaneous velocity field of the fluid flow by analyzing the particle motion. Although the current PIV method has achieved very impressive performance, the measurement accuracy of the PIV method is significantly influenced by the optical imaging technology and PIV measurement algorithms [4, 5]. Therefore, developing a high-accuracy PIV method remains a difficult task [6, 7].

Over the past few decades, various PIV measurement algorithms have been proposed and developed to improve the measurement accuracy of the PIV method. These methods can be classified into two main groups, namely, normalized cross-correlation (NCC) algorithms and optical flow algorithms [8]. NCC algorithms divide the first captured image into many fixed-size region-of-interest (ROI) windows and

*Corresponding author (email: huayang@hust.edu.cn)

assume that all the tracer particles in the same ROI window rigidly move within 1/4 of the window size. Meanwhile, the resolution of the velocity field estimated by NCC algorithms is also restricted by the window size [9, 10]. To overcome these limitations, optical flow algorithms are employed to estimate the optical field of two captured images as the velocity field of tracer particles, and they can provide a dense velocity field with high resolution [11].

Meanwhile, many optical imaging technologies have been developed for the PIV method to overcome the restrictions imposed by standard video signals (NTSC 30 fps/PAL 25 fps). The frame-straddling charge-coupled device (CCD) camera is the most popular optical imaging technology in the field of PIV measurements, such as combustion flow measurements, microflow field measurements, two-phase flow measurements, and so on [12]. Moreover, due to the development of high-frequency lasers, high-speed vision cameras that operate at 1000 fps or more have been effectively used in many time-resolved PIV applications to temporally resolve the relevant features of the flow field [13]. However, the interval times for both frame-straddling CCD cameras and high-speed cameras are predefined as a fixed interval time. Because the velocities of tracer particles in the unsteady flow field vary with time, the displacements of these tracer particles changes with time, when the time interval of capturing images is fixed. This means that the tracer particle in the first image may move out of the second image with large displacement, or may move within the image due to little displacement which is similar to the influence of noise. Thus, for unsteady flow field measurements, the use of a fixed interval time is not suitable for a wide range of velocity change and decreases the measurement accuracy of the conventional PIV method.

Real-time PIV has been widely applied in PIV and particle tracking velocimetry (PTV): examples include real-time particle tracking [14,15], real-time microscopic PIV [16,17], and real-time PIV for the turbulent bimodal wake [18]. However, these real-time methods are only based on hardware control or information regarding the current successive particle images. The available information of the current velocity field is limited, resulting in the situation that the estimated velocity is not sufficiently accurate. Thus, a novel real-time adaptive PIV method consists of imaging system and velocity estimation algorithm is necessary for the unsteady flows.

In this study, a RTA-PIV method is proposed to accurately measure the instantaneous velocity field of an unsteady flow field. In the proposed closed-loop RTA-PIV method, a new correlation-filter-based PIV measurement algorithm is introduced to calculate the velocity field in real time: it is very efficient especially for large-displacement movement. A Kalman predictor model, which has been widely used in particle image tracking [19–21], is established to predict the velocity of the next time instant and a suitable interval time of optical imaging system can be determined based on the predicted velocity. To adaptively adjust the interval time for capturing two particle images, a new high-speed frame-straddling vision system is developed for the proposed RTA-PIV method, and its time interval is not fixed as one pre-defined value and can vary with the velocity change at different time-instants.

The remainder of this paper is organized as follows. In Section 2, the proposed RTA-PIV method is introduced in detail, and the developed high-speed frame-straddling vision system is presented in Section 3. A range of numerical experiments on ground-truth image pairs and on real-world image sequences are reported and discussed in Section 4. In Section 5, the conclusions of this work are presented.

2 The proposed RTA-PIV method

2.1 The concept of the RTA-PIV method

In general, the conventional PIV method is an open-loop measurement method that acquires image pairs with a predetermined fixed interval time Δt. The displacement field $\Delta \boldsymbol{s}$ between the ROI windows $\boldsymbol{r}_i(x, y)$ and $\boldsymbol{r}'_i(x, y)$ is then calculated by the traditional PIV algorithm, and the average velocity during the interval time is calculated by $\overline{\boldsymbol{w}} = \Delta \boldsymbol{s}/\Delta t$. However, for the instantaneous velocity $\boldsymbol{w}$, the equation is

$$\boldsymbol{w} = \lim_{\Delta t \to 0} \frac{\Delta \boldsymbol{s}}{\Delta t}. \tag{1}$$

As shown in eq. (1), the shorter the interval time Δt is, the closer the average velocity $\overline{\boldsymbol{w}}$ is to the instantaneous velocity $\boldsymbol{w}$, where $\boldsymbol{w} = (u, v)$, u is the velocity in the horizontal direction, and v is the velocity in the vertical direction.

However, in the actual PIV experiment, when the interval time is shorter, the displacement of the particles is smaller, and the influence of noise information on the correlation peak is much larger than that of small displacements. Additionally, the correlation peak is generally too sharp to allow for a reliable sub-pixel estimation of the displacement. When the interval time is longer, the signal strength of the correlation peak will decrease with increasing displacements due to the proportional decrease in possible particle matches. For a PIV experiment with a steady flow field, we can choose an optimal fixed interval time based on many experimental results. However, for an unsteady flow field, a fixed interval time is not satisfactory, and a series of fixed intervals cannot be set in advance because the unsteady characteristics of the flow field cannot be predicted. The existing PIV methods generally choose the interval time through a predetermined

fixed value or N predetermined values, which cannot meet the needs of the application in the unsteady flow field measurement with a relatively high measurement accuracy. Therefore, a PIV method with adaptive adjustment of the interval time is imperative to accurately measure the instantaneous velocity field of the unsteady flow field.

As shown in Figure 1, the proposed RTA-PIV method is a closed-loop method that acquires image pairs with the interval time adaptively adjusted by the instantaneous velocity of the unsteady flow field. First, an online velocity initialization process is performed to obtain the sequence of velocity fields, this online initialization is a conventional PIV method that uses a novel correlation-filter-based PIV (CF-PIV) measurement algorithm with a predetermined fixed interval time. Then, the vector fields $\hat{\boldsymbol{w}} = (\hat{u}, \hat{v})$ at the next time t_{n+1} are predicted through the velocity field sequence, the optimal interval time Δt_{n+1} at time t_{n+1} is evaluated, and the high-speed frame-straddling vision system captures image pair $[\boldsymbol{I}(t_{n+1}), \boldsymbol{I}(t'_{n+1})]$ instantaneously, where $t'_{n+1} = t_{n+1} + \Delta t_{n+1}$. Subsequently, a new velocity field is evaluated using the correlation-filter-based PIV measurement algorithm with an adaptive interval time. This velocity field at time t_{n+1} is more accurate than all previous velocity fields evaluated by the conventional PIV method because of the successive optimal interval time Δt_{n+1}. Finally, the velocity field sequence and related parameters used in the prediction are updated, and a new closed-loop cycle restarts.

The image pair with adaptive interval time is capable of offering various sets of meaningful correlation peaks, and thus, there exists a possibility of compensating for the loss due to the low image quality. Furthermore, time-related properties can be revealed in concert with the chronological particle images.

2.2 Adaptive interval time adjustment algorithm

The proposed interval time prediction algorithm is a closed-loop method that combines a correlation filter and Kalman predictor. The CF-PIV measurement algorithm computes the velocity field, which will be described in detail in the next subsection, and the Kalman predictor predicts the velocity at the next time instant, which will be described in this subsection. The Kalman predictor is a recursive estimator that implements a time-varying estimation in non-stationary time-varying signal processing. Because of the use of the recursive strategy, there is no need to consider many past input signals, and only the previous input signal is considered in each recursive operation: that is, the predictor does not need to save the measured values of the past, and so the velocity can be predicted in real time.

The Kalman predictor model consists of two parts: prediction and correction. The Kalman predictor is an online processing in which new observations are processed as soon as they are calculated. For a time-varying system, we first define a set of state space equations: state equation (or prediction equation) and observation equation (or correction equation).

Assuming that $\boldsymbol{w}_{n+1}$ represents the predictive velocity vector at time t_{n+1}, $\boldsymbol{w}_{n+1} = (u_{n+1}(x, y), v_{n+1}(x, y))$ is the ve-

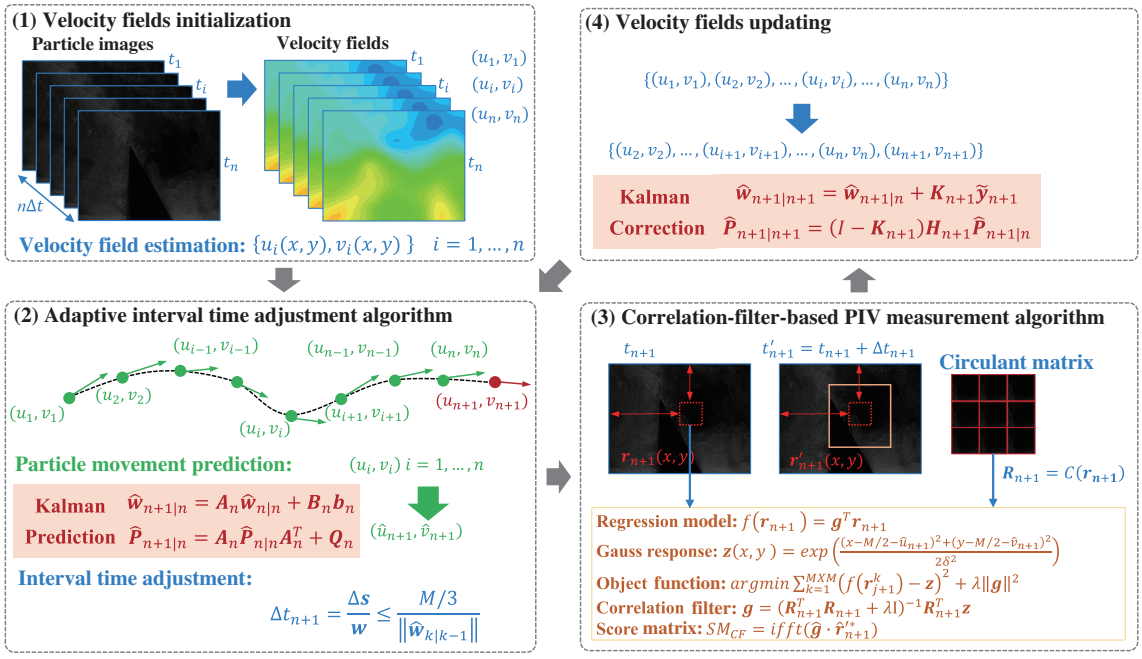

Figure 1 (Color online) A flowchart of the proposed closed-loop RTA-PIV method.

locity vector of fluid in the coordinate position (x, y), and $\boldsymbol{W}_{n+1}$ is the measured vector of the velocity field using the correlation-filter-based velocity estimation that will be described in detail in the next subsection.

$$\boldsymbol{w}_{n+1} = \boldsymbol{A}_n \boldsymbol{w}_n + \boldsymbol{B}_n \boldsymbol{b}_n + \boldsymbol{q}_n, \tag{2}$$

$$\boldsymbol{W}_{n+1} = \boldsymbol{H}_{n+1} \boldsymbol{w}_{n+1} + \boldsymbol{d}_{n+1}. \tag{3}$$

The first is the state equation and the other is the observation equation. $\boldsymbol{A}_n$ is the state transition matrix, $\boldsymbol{B}_n$ is the control matrix, $\boldsymbol{b}_n$ is the control vector, $\boldsymbol{q}_n$ is systematic error (noise), $\boldsymbol{H}_{n+1}$ is the measurement matrix and $\boldsymbol{d}_{n+1}$ is measurement error (noise). The state transition matrix $\boldsymbol{A}_n$, control matrix $\boldsymbol{B}_n$ and measurement matrix $\boldsymbol{H}_{n+1}$ are uncertain and can be calculated by the velocity field sequence $\{u_i, v_i\}$ $(i = 1, 2, ..., n)$ obtained in the previous initialization process. The control vector $\boldsymbol{b}_n$ is generally set to a unit vector, and $\boldsymbol{q}_n$ and $\boldsymbol{d}_{n+1}$ are Gaussian noise:

$$\boldsymbol{q}_n \sim N(0, \boldsymbol{Q}_n), \tag{4}$$

$$\boldsymbol{d}_{n+1} \sim N(0, \boldsymbol{D}_{n+1}). \tag{5}$$

The whole Kalman prediction process is a recursive calculation process, "prediction-correction-prediction-correction..." continuously. $\hat{\boldsymbol{w}}$ represents the predicted state velocity, $\hat{\boldsymbol{P}}$ is the predicted minimum mean square error matrix, and the prediction equations are

$$\hat{\boldsymbol{w}}_{n+1|n} = \boldsymbol{A}_n \hat{\boldsymbol{w}}_{n|n} + \boldsymbol{B}_n \boldsymbol{b}_n, \tag{6}$$

$$\hat{\boldsymbol{P}}_{n+1|n} = \boldsymbol{A}_n \hat{\boldsymbol{P}}_{n|n} \boldsymbol{A}_n^{\mathrm{T}} + \boldsymbol{Q}_n, \tag{7}$$

where $\hat{\boldsymbol{w}}_{n+1|n}$ is the predicted state velocity at time t_{n+1} and $\hat{\boldsymbol{P}}_{n+1|n}$ is the covariance based on $\hat{\boldsymbol{P}}_{n|n}$ calculated with $\boldsymbol{Q}_n$ at time t_n.

We then calculate the optimal interval time Δt_{n+1} of the optical imaging system at the next time instant t_{n+1} through the predicted velocity value obtained by the Kalman predictor. Considering the limitations of the ROI window in the CF-PIV measurement algorithm, the interval time Δt_{n+1} at the next time instant t_{n+1} should meet the following requirement:

$$\Delta t_{n+1} \leq \frac{1}{3} \cdot \frac{M}{\left\| \hat{\boldsymbol{w}}_{n+1|n} \right\|}, \tag{8}$$

where M is a fixed window size related to the correlation-filter-based PIV measurement algorithm that we use. The coefficient in the traditional PIV algorithm is 1/3 not 1/4 because of the good performance of CF-PIV on large-displacement movements. Finally, the high-speed frame-straddling vision system instantaneously captures image pair $[\boldsymbol{I}(t_{n+1}), \boldsymbol{I}(t'_{n+1})]$, and the CF-PIV measurement algorithm computes the velocity field at the next time instant t_{n+1} using image pair $[\boldsymbol{I}(t_{n+1}), \boldsymbol{I}(t'_{n+1})]$.

2.3 Correlation-filter-based PIV measurement algorithm

In this study, we consider velocity field measurements of particle images from the new perspective of visual object tracking, and we replace cross-correlation with kernel correlation filter (KCF) [22], which exhibits excellent comprehensive performance, particularly for tolerating large-displacement movements, because the circulant-matrix operation can decrease the error caused by the periodicity assumption of fast Fourier transform (FFT) [23].

The integral formulation of the score matrix in the discrete cross-correlation function is described as follows:

$$SM_{\mathrm{DCC}}(x, y) = \sum_{i=-\frac{M}{2}}^{\frac{M}{2}} \sum_{j=-\frac{M}{2}}^{\frac{M}{2}} \boldsymbol{r}(i, j) \boldsymbol{r}'(i + x, j + y). \tag{9}$$

The variables $\boldsymbol{r}$ and $\boldsymbol{r}'$ are the sample ROIs extracted from the image pair $[\boldsymbol{I}(t_{n+1}), \boldsymbol{I}(t'_{n+1})]$, and M is the size of the ROI window of the samples. The alternative to calculating the cross-correlation directly with eq. (9) is to take advantage of the correlation theorem, which states that the cross-correlation of two functions is equivalent to a complex conjugate multiplication of their Fourier transforms:

$$SM_{\mathrm{FFT}} = ifft(\hat{\boldsymbol{r}} \cdot \hat{\boldsymbol{r}}'^{*}), \tag{10}$$

where $\hat{\boldsymbol{r}}$ and $\hat{\boldsymbol{r}}'$ are the Fourier transforms of the sample ROIs $\boldsymbol{r}$ and $\boldsymbol{r}'$, respectively; the superscript * denotes the conjugate; and $ifft$ is the inverse Fourier transform. However, the measurement range is limited to the size of the ROI window. To improve the measurement range, the pyramid strategy and image warping operation are used, which have greatly reduced the computational efficiency. In the CF-PIV measurement algorithm, the pyramid strategy is unnecessary because it is very efficient, particularly for large-displacement movements.

The process of the correlation-filter-based PIV measurement algorithm is as follows. First, generate a circulant matrix $\boldsymbol{R}_{n+1}$ of the sample ROI $\boldsymbol{r}_{n+1}$:

$$\boldsymbol{R}_{n+1} = C(\boldsymbol{r}_{n+1}). \tag{11}$$

The circulant matrix uses the method of dense sampling to utilize the features of the sample ROI. This only is more efficient for obtaining the characteristics of the input images but also greatly increases the number of samples of the filter model, thereby increasing the discriminability of the filter. In circulant matrix $\boldsymbol{R}_{n+1}$, the number of samples is $M \times M$, and the size of each sample is the same as the sample ROI $\boldsymbol{r}_{n+1}$. Additionally, the regression model of correlation filter $\boldsymbol{g}$ is

$$f(\boldsymbol{r}_{n+1}) = \boldsymbol{g}^{\mathrm{T}} \boldsymbol{r}_{n+1}. \tag{12}$$

Then, generating a Gauss response matrix $\boldsymbol{z}$ whose size is the same as $\boldsymbol{r}$, the Gauss response matrix $\boldsymbol{z}$ is a discrete form of the two-dimensional Gauss distribution:

$$z(x,y)=\exp\left(-\frac{\left(x-\frac{M}{2}-\hat{u}_{n+1}\right)^2+\left(y-\frac{M}{2}-\hat{v}_{n+1}\right)^2}{2\delta^2}\right), \tag{13}$$

where exp is an exponential function based on a natural constant, x and y are image coordinates in $\boldsymbol{r}$, $\hat{u}_{n+1}$ and $\hat{v}_{n+1}$ are predicted velocities at position (x,y) at time instant t_{n+1}, the initial values of $\hat{u}_1$ and $\hat{v}_1$ are set as 0, and σ is the variance of the Gaussian kernel in the x direction and y direction. The objective function of the regression model is

$$\arg\min_{\boldsymbol{g}} \sum_{k=1}^{M\times M}\left(f(\boldsymbol{r}_{n+1}^k)-z\right)^2+\lambda\|\boldsymbol{g}\|^2, \tag{14}$$

$\boldsymbol{r}_{n+1}^k$ is a sample in the circulant matrix $\boldsymbol{R}_{n+1}$, where $k=1,...,M\times M$. Additionally, λ is the coefficient of the regularization term of the regression model, and it is used to ensure the generalization ability of the classifier. Eq. (14) can be expressed directly in matrix form as follows:

$$\arg\min_{\boldsymbol{g}}\left(|\boldsymbol{R}_{n+1}\boldsymbol{g}-z|^2+\lambda|\boldsymbol{g}|^2\right). \tag{15}$$

Letting the derivative of eq. (15) be 0, the following can be obtained:

$$\boldsymbol{g}=(\boldsymbol{R}_{n+1}^{\mathrm{T}}\boldsymbol{R}_{n+1}+\lambda I)^{-1}\boldsymbol{R}_{n+1}^{\mathrm{T}}z. \tag{16}$$

According to the characteristics of the circulant matrix in the frequency domain, all the circulant matrices can be transformed into diagonal matrices in the frequency domain through a Fourier transform, and the convolution calculation in the time domain is transformed into a point multiplication in the frequency domain. Eq. (16) can be transformed into the following form:

$$\hat{\boldsymbol{g}}=\frac{\hat{\boldsymbol{r}}_{n+1}\cdot\hat{\boldsymbol{z}}}{\hat{\boldsymbol{r}}_{n+1}^*\cdot\hat{\boldsymbol{r}}_{n+1}+\lambda}, \tag{17}$$

where $\hat{\boldsymbol{g}}$ and $\hat{\boldsymbol{z}}$ are the Fourier transforms of the correlation filter $\boldsymbol{g}$ and Gauss response matrix $\boldsymbol{z}$, respectively.

$$SM_{\mathrm{CF}}=ifft(\hat{\boldsymbol{g}}\cdot\hat{\boldsymbol{r}}'^*_{n+1}). \tag{18}$$

Finally, the correlation filter $\boldsymbol{g}$ acts on $\boldsymbol{r}'_{n+1}$, the corresponding area on the second image, and the score matrix SM_{CF} is generated; then, the score matrix SM_{CF} is transformed to the time domain, and the maximum response position is selected as the displacement, similar to the traditional cross-correlation-based PIV measurement algorithms.

2.4 Velocity fields updating

High-accuracy velocity field (u_{n+1},v_{n+1}) is evaluated by the CF-PIV measurement algorithm at time instant t_{n+1}, and the measured vector of the velocity field is $\boldsymbol{W}_{n+1}=(u_{n+1},v_{n+1})$. In the velocity field updating process, the velocity field sequence $\{u_i,v_i\}$ $(i=1,2,...,n)$ is updated by $\{u_i,v_i\}$ $(i=2,3,...,n+1)$, which is used to update the state transition matrix $\boldsymbol{A}_n$, control matrix $\boldsymbol{B}_n$ and measurement matrix $\boldsymbol{H}_{n+1}$ in the Kalman predictor model.

Then, in the Kalman correction process, the measurement residual $\tilde{\boldsymbol{y}}_{n+1}$, the measurement covariance $\boldsymbol{S}_k$ and the Kalman gain $\boldsymbol{K}_k$ are calculated by

$$\tilde{\boldsymbol{y}}_{n+1}=\boldsymbol{W}_{n+1}-\boldsymbol{H}_{n+1}\hat{\boldsymbol{w}}_{n+1|n}, \tag{19}$$

$$\boldsymbol{S}_{n+1}=\boldsymbol{H}_{n+1}\hat{\boldsymbol{P}}_{n+1|n}\boldsymbol{H}_{n+1}^{\mathrm{T}}+\boldsymbol{D}_{n+1}, \tag{20}$$

$$\boldsymbol{K}_{n+1}=\hat{\boldsymbol{P}}_{n+1|n}\boldsymbol{H}_{n+1}^{\mathrm{T}}\boldsymbol{S}_{n+1}^{-1}, \tag{21}$$

where $\tilde{\boldsymbol{y}}_{n+1}$ is the measurement residual at time t_{n+1}, and $\boldsymbol{K}_{n+1}$ is the Kalman gain to combine $\hat{\boldsymbol{w}}_{n+1|n}$ with $\tilde{\boldsymbol{y}}_{n+1}$ to obtain the next predicted displacement. Then, the predicted state velocity $\hat{\boldsymbol{w}}$ and the predicted minimum mean square error matrix $\hat{\boldsymbol{P}}$ are corrected by

$$\hat{\boldsymbol{w}}_{n+1|n+1}=\hat{\boldsymbol{w}}_{n+1|n}+\boldsymbol{K}_{n+1}\tilde{\boldsymbol{y}}_{n+1}, \tag{22}$$

$$\hat{\boldsymbol{P}}_{n+1|n+1}=(I-\boldsymbol{K}_{n+1})\boldsymbol{H}_{n+1}\hat{\boldsymbol{P}}_{n|n}. \tag{23}$$

The algorithms in the proposed RTA-PIV method mainly include the adaptive interval time adjustment algorithm and CF-PIV measurement algorithm. First, an online velocity field initialization process is performed to obtain the sequence of velocity fields $\{u_i,v_i\}$ $(i=1,2,...,n)$. Then, the Kalman predictor is used to predict the velocity of the next time instant $\hat{\boldsymbol{w}}_{n+1|n}$, and the suitable interval time Δt_{n+1} at the next time instant t_{n+1} can be determined based on the predicted velocity $\hat{\boldsymbol{w}}_{n+1|n}$. Subsequently, the high-speed frame-straddling vision system captures the image pair with Δt_{n+1} instantaneously, and we use the CF-PIV measurement algorithm to calculate the high-accuracy velocity field $\hat{\boldsymbol{W}}_{n+1}$ at time instant t_{n+1}. Finally, the velocity field sequences are updated, the related parameters of the Kalman predictor are corrected, and a new closed-loop cycle restarts.

2.5 Parameter settings

For the proposed RTA-PIV method, there are several important parameters. In the CF-PIV measurement algorithm, the step affects the density of the velocity field, and it is generally set as half of the window size. The size of the Gauss response matrix $\boldsymbol{g}$ is the same as the window size, the variance σ is set as 0.1, the regularization coefficient λ is set as 10^{-5}, and the number of image pairs for velocity field initialization is set as

4. In the adaptive interval time adjustment algorithm, the initial state transition matrix and the control matrix are both set as identity matrices, the initial velocity estimation is given by online initialization, and the systematic noise and the measurement noise are adapted as a result. The relative value between the systematic noise and the measurement noise is important. If the systematic noise is set to be larger than the measurement noise, then the Kalman predictor will bias the measured value; otherwise, the Kalman predictor will bias the predicted value. The value should be set according to the actual situation. In the simulation experiment, we set the systematic noise as 0.0025 and the measurement noise as 0.001.

3 High-speed frame-straddling vision system

To adaptively adjust the interval time between two captured particle images, a new high-speed frame-straddling vision system is developed for the proposed RTA-PIV method, which consists of a high-speed frame-straddling camera (HFC) and a high-speed image processor (HIP).

The HFC is used to generate the trigger signal to control the exposure of the two scientific complementary metal-oxide semiconductor (sCMOS) sensors and the double-pulsed laser to adjust the real-time adaptive interval time for calculating the unsteady flow field. The HFC mainly consists of three parts: spectral region, control unit, and transmission unit, as shown in Figure 2(a). Figure 2(b) is a function block diagram of the HFC, and the specifications of the sCMOS sensor used in the HFC are: two CIS2521 sensors, the maximum of resolution is 2560×2160 pixels, pixel size of $6.5\ \mu m \times 6.5\ \mu m$, and dynamic range larger than 83.5 dB.

In the HFC, a field programmable gate array (FPGA) controls the exposure of the two sCMOS sensors. To reduce the magnitude of the interval time, a spectral region and the HFC divide the incident light evenly into two parts and then transmit it to rear sCMOS sensors through the spectral region, as shown in Figure 2(a). The function of the flange extender is to extend the optical path and allow the imaging plane to fall on the sensor. With the spectral region, there is almost no loss of luminous flux, and it is ensured that the brightness obtained by the two sensors has consistent exposure at the same time.

The image data buffering and transmission process is shown in Figure 2(b). On FPGA, through the multiplexer (MUX), reset first input first output (RST_FiFo) and data first input first output (Data_FiFo), the images data composed of F_Sensor1, L_Sensor1, F_Sensor2, and L_Sensor2 are transmitted to the FPGA. Then, the FPGA transmits it to double data rate three (DDR3) to buffer the data, receives it from DDR3 and transmits it to a CameraLink through a memory interface generator (MIG) and differential FiFo (Diff_FiFo). Then, 64-bit gray-level images can be transferred from each of the two sCMOS sensors at 500 fps (for 1024×1024 pixels) or 100 fps (for 2560×2160 pixels). After the delay module receives the interval time of the next frame from HIP, FPGA generates four trigger signals: two to control the exposure of the two sCMOS sensors, and the other two to control the operation of the double-pulsed laser through the delay module. Because the system clock is 287 MHz, the precision of the triggers can be accurate to nanoseconds, and the minimum interval time is 10 ns. Conversely, the interval time of the traditional PIV camera can only be 100 ns.

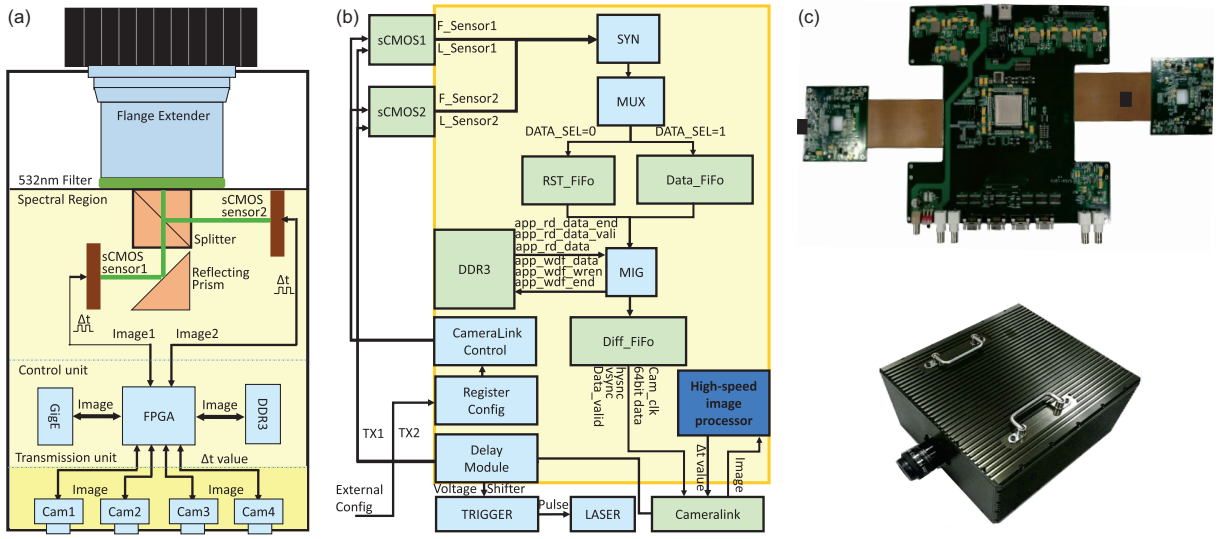

Figure 2 (Color online) High-speed frame-straddling vision system. (a) The interval structure and the general flow chart of the HFC; (b) the function block diagram of HFC; (c) from top to bottom are the physical map and mechanical enclosure of HFC, respectively.

The physical map of the HFC is shown in Figure 2(c). The FPGA and two sCMOS sensors are connected with two soft boards. Through the application of splitting, sCMOS sensors and FPGA control unit, the HFC realizes interval time adjustment and low-light sensitivity, whereas the interval time of the traditional frame-straddling camera is a predefined fixed value. Consequently, the HFC could more accurately measure the velocity of unsteady flows.

The high-speed frame-straddling vision system is a high-speed vision system for high-frame-rate image capturing, processing, and adjustment of the interval time. Figure 3(a) shows the general configuration of the whole system. First, frame-straddling images captured by the HFC are transferred to the high-speed image processor (HIP) which mainly consists of a FPGA, two digital signal processings (DPSs) and four graphics processing units (GPUs), and all the RTA-PIV algorithms are implemented here. Then, HIP calculates the interval time of the next time instant and transmits it to the HFC. Finally, the FPGA of the HFC generates four path triggering signals: two channels controlling two sCMOS sensors for exposure, and the other two controlling the double-pulsed laser sending out a pulsed laser.

4 Simulation and experiment

4.1 Simulation: Performance comparison of CF-PIV algorithm

To illustrate the accuracy of the proposed correlation filter approach in the different situations, we compare several methods with respect to the Visualization Society of Japan (VSJ) dataset [24]. Five algorithms are compared: two correlation PIV methods, two optical flow algorithms, and our algorithm. These algorithms are: window displacement iterative multigrid 32 (WIDIM32) with an interrogation window that is set as 32×32 [25], size and shape adaptation method (SSAM) [26], variational optical flow for particle image velocimetry (VOF-PIV) [27], integrated continuity equation based optical flow for PIV (ICE-PIV) [28] and the proposed method CF-PIV32 which is based on a correlation filter with a 32×32 interrogation window. The initial and final window size of WIDIM32 and CF-PIV are both 32×32 and the number of iterative pass is set to 3. After obtaining the estimated velocity, all velocity fields are culled spurious vectors using median filter with a size of 5×5. This strategy is used for all experiments in this paper. The average relative L_1 norm error is used to compare the different motion fields.

Figure 3(b) shows that the results achieved from cases {#1,#2,#3,#5,#6,#7,#8} are the best for algorithm CF-PIV32 which we proposed compared with other methods. Additionally, on case #4, the average relative L_1 norm error of CF-PIV32 is larger than that of SSAM, which is widely used in unsteady flow fields. The poor result obtained with the proposed technique, compared with SSAM on #4, can be explained by the interrogation window size of CF-PIV32 (the higher the density of image pairs, the smaller the interrogation window size that is needed for the calculation of case #4). For case #4, although CF-PIV32 is slightly less than SSAM, it is high enough to calculate the velocity field compared with three other methods: WIDIM32, VOF-PIV and ICE-PIV. Moreover, on cases {#6,#7,#8}, the L_1 of CF-PIV32 is close to 0.15%, while the others are close to 0.5% or more, which shows that the proposed method offers great advantages with respect to particle diameter and out-of-plane velocity and is better at avoiding interference than SSAM.

Referring to Figure 3(b), one can find that CF-PIV32 provides better results irrespective of the displacement of the flow field, the number of particles or out-of-plane velocity. From the above, CF-PIV32 can resolve the eight VSJ standard image pairs better and has a wider range of use in complex flow fields, particularly in measuring large displacements.

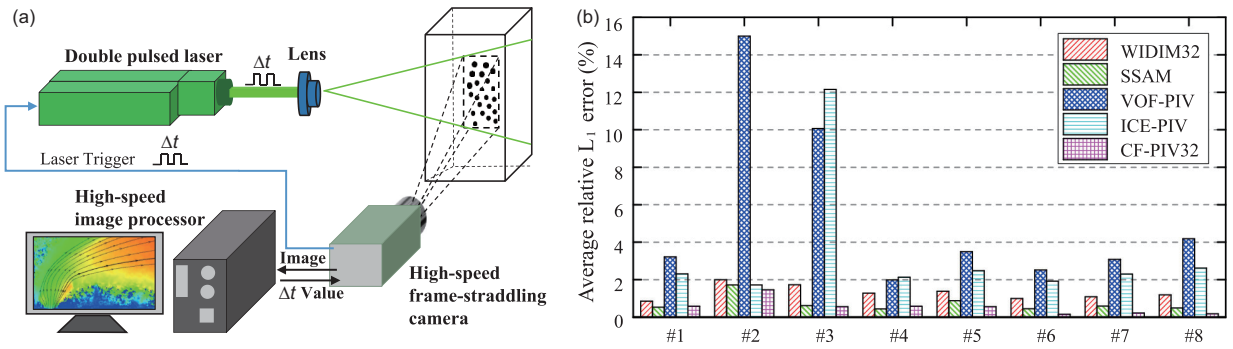

Figure 3 (Color online) (a) Implementation of the proposed closed-loop RTA-PIV method in the high-speed frame-straddling vision system; (b) average relative L_1 errors of five algorithms. From left to right (and top to bottom in the legend): WIDIM32, SSAM, VOF-PIV, ICE-PIV, and the proposed method CF-PIV32.

4.2 Simulation: Performance comparison of RTA-PIV method

To verify the feasibility and superiority of RTA, we design three simulation experiments in this section. A simple simulation on a 1-D flow field is generated, in which the ground-truth velocity is the same spatially and changing sinusoidally over time. In the first case, only the frequency gradually increases, in the second case, only the amplitude gradually increases, and the third case is a superposition of the first case and the second case, in which the frequency and amplitude change simultaneously. The velocity changes of the three cases are shown in Figure 4(a). Four algorithms are compared: WIDIM32 without RTA, CF-PIV32 without RTA, WIDIM32 with RTA and CF-PIV32 with RTA. The root mean square error (RMSE) is used to compare the performances of these methods in the three simulation experiments.

The results of the three simulation experiments are shown in Figure 4(b)–(d). Overall, we can observe that the traditional method WIDIM32 without RTA has the maximum RMSE among these four methods. At the same time, for CF-PIV32 without RTA, the RMSE is slightly smaller than that of the traditional method WIDIM32 without RTA, but the error is still large. After introducing the Kalman predictor, the interval times of WIDIM32 and CF-PIV32 vary with time according to be WIDIM32 with RTA and CF-PIV32 with RTA. As shown in Figure 4(b)–(d), in different cases, the two improved methods can effectively reduce the RMSE and measure the velocity value of the velocity field at all times. In particular, CF-PIV32 with RTA is better, whose error is always the lowest.

This result also indicates that when the frequency or amplitude increases, the methods without RTA have a larger RMSE because the velocity is changing more drastically and the fixed time is not suitable under this circumstance. When introducing the RTA method, the RMSE is greatly reduced and almost does not change as the velocity changes. From the above, we can draw the conclusion that CF-PIV32 offers better performance than the traditional WIDIM32 method under the same conditions, and when the methods are introduced with RTA, the errors of the two methods are greatly reduced, and CF-PIV32 with RTA has the lowest RMSE.

4.3 Experiment: Unsteady microflow field

To illustrate the generalization of the proposed method in a microflow field, we perform a micro-PIV experiment, as shown in Figure 5(a). Orange fluorescent particles with diameter of 0.3 μm are dispersed in distilled water and stored in a syringe. A New Era NE-1000 injection pump drives the syringe with a variable rate. The flow field is within a microfluidic chip, whose cross-section is 30 μm wide × 28 μm deep. The whole flow field is illuminated using a fluorescent light (Nikon IntensiLight C-HGFI) with a wavelength of

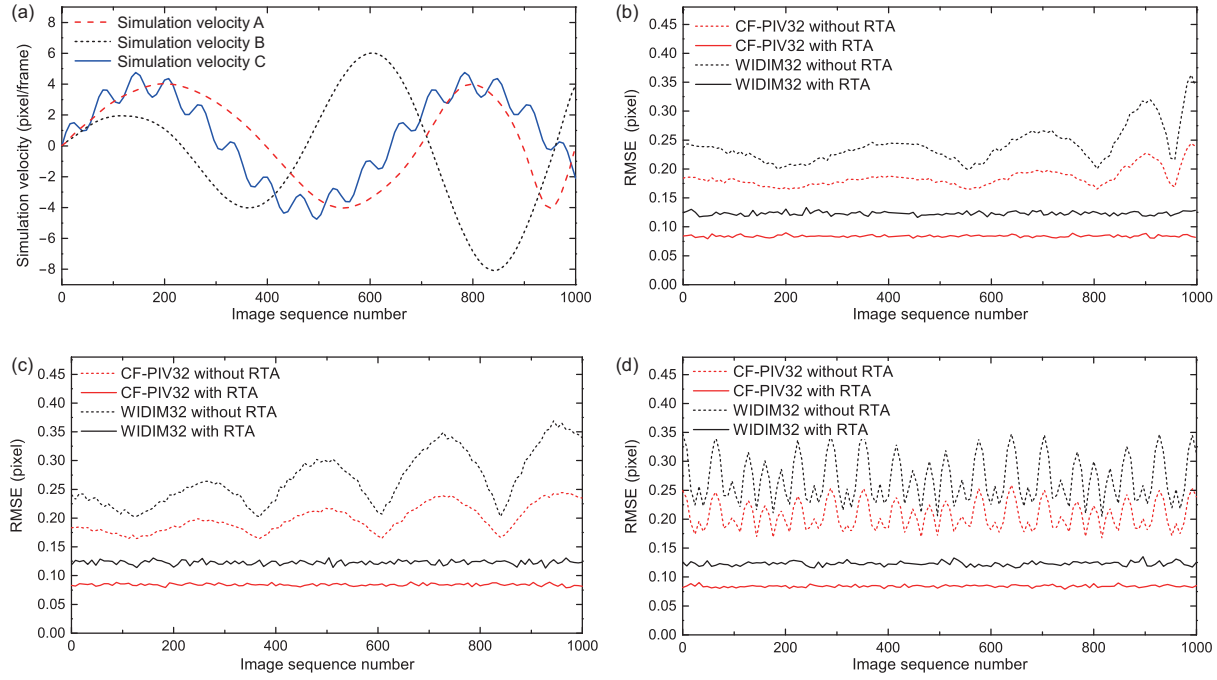

Figure 4 (Color online) Our simulation experiment settings and results. (a) The changing of the velocities of three cases; (b) the performances under the case of changing frequency only; (c) the performances under the case of changing amplitude only; (d) the performances under the case of changing frequency and amplitude simultaneously.

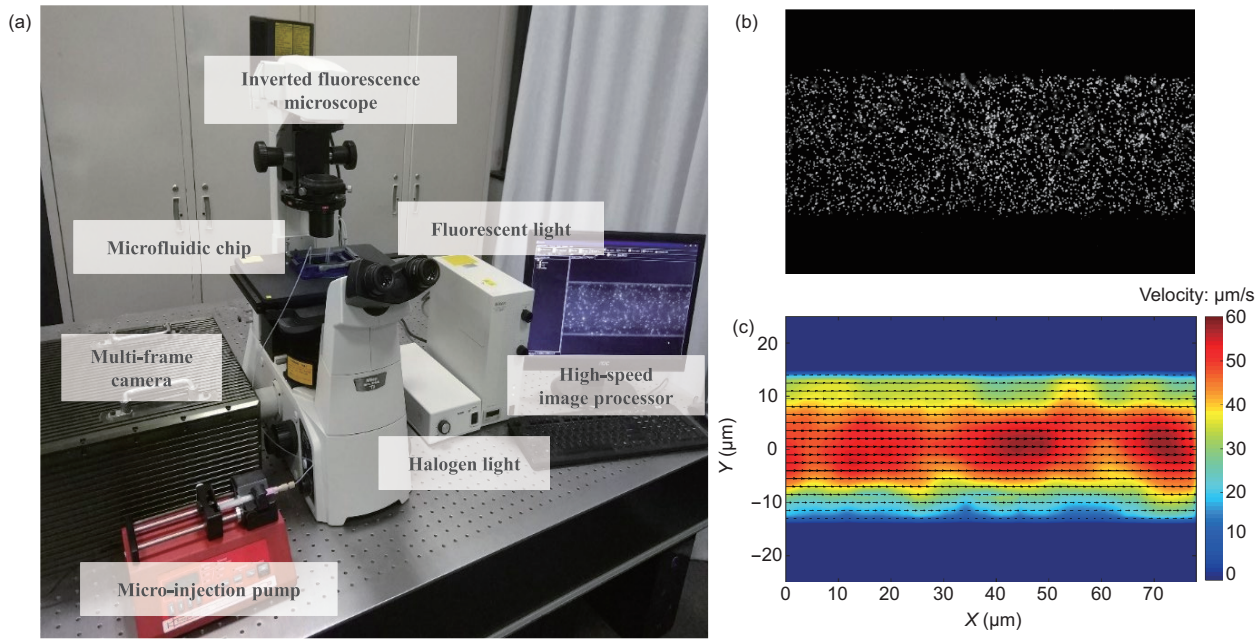

Figure 5 (Color online) (a) Micro-PIV experimental platform; (b) the PIV images of unsteady micro-PIV flow at 10.396 s; (c) the energy map and the vector map of unsteady Micro-PIV flow at 10.396 s with the interval time of 15 ms.

532 nm and imaged by a Nikon Eclipse Ti-S inverted fluorescent microscope with a 60× magnification lens. The field is captured using an HFC with a frame rate of 30 Hz. The flow field that we set is a laminar flow field, and to make the field smooth and more complicated, we set a velocity that changes within a series of cubic curves (three curves), and these curves are smoothly connected at 5.033 and 10.396 s. In the experiment, we compare the performances of the CF-PIV32 and WIDIM32 method with RTA and with a fixed interval time.

The PIV image is shown in Figure 5(b). The result of the proposed algorithm CF-PIV32 with RTA at the moment of 10.396 s is shown through the energy map and the velocity vector map, as in Figure 5(c). As shown in Figure 5(c), the maximum speed of the flow occurs in the center of the pipe, and the minimum is at the boundary of the pipe, which is consistent with the situation in laminar flow fields. At this moment, the mainstream velocity measured is red, which is approximately 59.78 μm/s, whose theoretical value is 58.36 μm/s, and the error with respect to the theoretical velocity equals to be 2.43%.

The time-velocity curves of these cases are shown in Figure 6(a), and the corresponding average relative L_1 errors are shown in Figure 6(b). As shown in Figure 6(b), in the large fixed interval time (25 ms), the computational error begins when the speed is greater than approximately 50 μm/s, and in the small fixed interval time (10 ms), the computational error begins when the speed is approximately less than 28 μm/s; thus, the fixed interval time is not suitable for the velocity field at all the times. The initial interval time of RTA-PIV is set to be 30 ms, and the interval time is adjusted during the entire experiment: for example, the interval time is adjusted to 28, 15, and 29 ms at 4, 10, and 16 s.

Thus, the fixed interval time is not suitable for the unsteady flow field, and CF-PIV32 with RTA can adapt the interval time and perfectly suit the flow field measurement at all times. The CF-PIV32 algorithm can perfectly obtain the distribution of velocity in the unsteady microflow field, and the error is smaller than that of the WIDIM32 algorithm overall in the same case. When applying the adaptive interval time adjustment method, the error caused by an inappropriate interval time can be greatly reduced.

4.4 Experiment: Unsteady low speed jet flow field

To illustrate the importance of the adaptive interval time adjustment in the proposed method, we perform a low speed jet flow experiment as shown in Figure 7. The TiO_2 particles are dispersed in the flow field by a solid particle generator, and their diameter is approximately 20 μm. The particles are then illuminated using a continuous laser (LWGL532) with a wave length of 532 nm, and captured using a HFC with a frame rate of 40 fps. The field of view covers approximately 40 mm × 75 mm on 512 pixel × 966 pixel. In the experiment we compare the CF-PIV32 with RTA and with fixed time, and the result of these methods are shown through the energy map and the vector map.

The PIV images are displayed in the first column

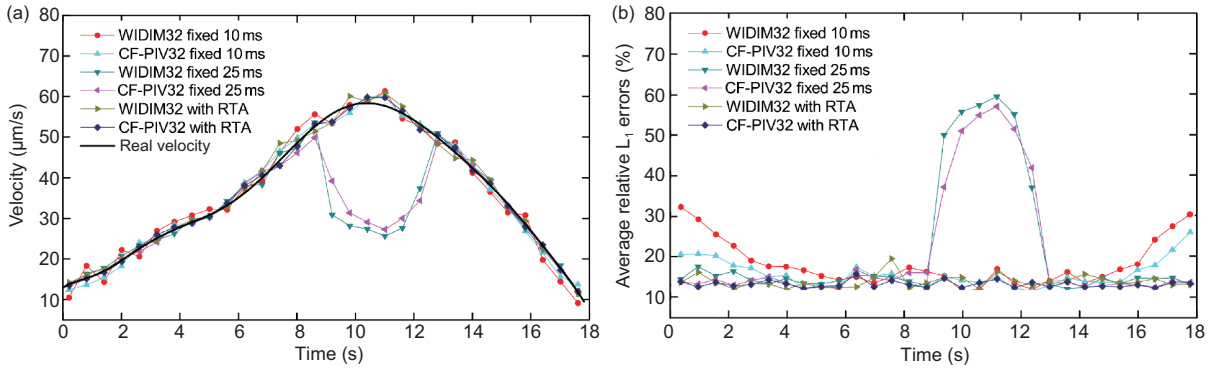

Figure 6 (Color online) (a) The time-velocity curves of CF-PIV32 and WIDIM32 with RTA and with fixed interval time (10 and 25 ms); (b) the average relative L_1 errors of CF-PIV32 and WIDIM32 with RTA and with fixed interval time (10 and 25 ms).

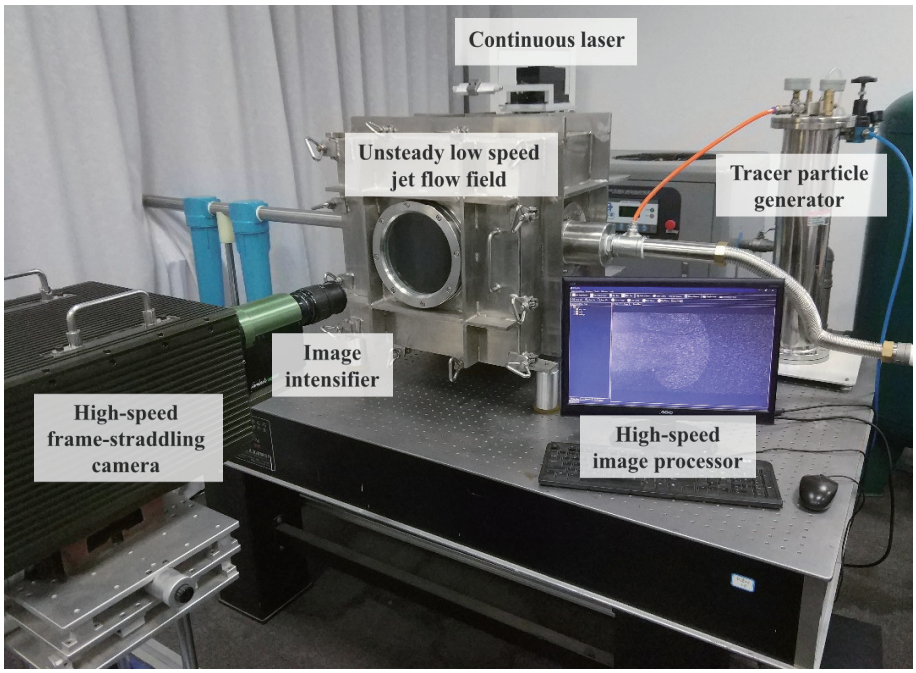

Figure 7 (Color online) Low speed jet experimental platform consisting of six parts: continuous laser, unsteady low speed jet flow field, tracer particle generator, image intensifier, high-speed frame-straddling camera and high-speed image processor.

(Figure 8(a), (c), (e)). The proposed algorithm CF-PIV32 with RTA is used to calculate the velocity field of this low speed flow field and the results are shown through the energy map and the velocity vector map, as shown in the second column (Figure 8(b), (d), (f)). Through the adjustment of interval time which is set to 2 ms with RTA, the final interval time is adjusted to 0.98, 1.07, 1.24 ms at 0.3, 0.5 and 0.7 s, respectively. Therefore, CF-PIV32 with RTA can be perfectly suited to the measured flow field all times.

To illustrate the importance of RTA, we remove it and set the proposed algorithm CF-PIV32 with fixed interval time. The results of fixed interval time 0.5 and 2 ms are shown in Figure 9. When the interval time is short, the small displacement causes a large number of calculation error vectors, as showed in the vortex below the jet in Figure 9(a), and the structure of the jet is not fully displayed in Figure 9(e). When the interval time is long, the large displacement exceeds the size of the ROI window and cannot be measured, as showed in Figure 9(b). From the energy map we can observe that the flow is unsteady, and the velocity field is gradually expanding from left to right, first increasing and then reducing with the increasing distance. Overall, the speed of flow decreases over time. Furthermore, the velocity maps reveal that at the end of the jet, there are two vortices on both side of the mainstream. For the first case, the mainstream velocity measured is red which is approximately 0.87 m/s whose theoretical value is 0.88 m/s. The error with respect to the theoretical velocity is 1.14%. Therefore, if the time interval is fixed, the

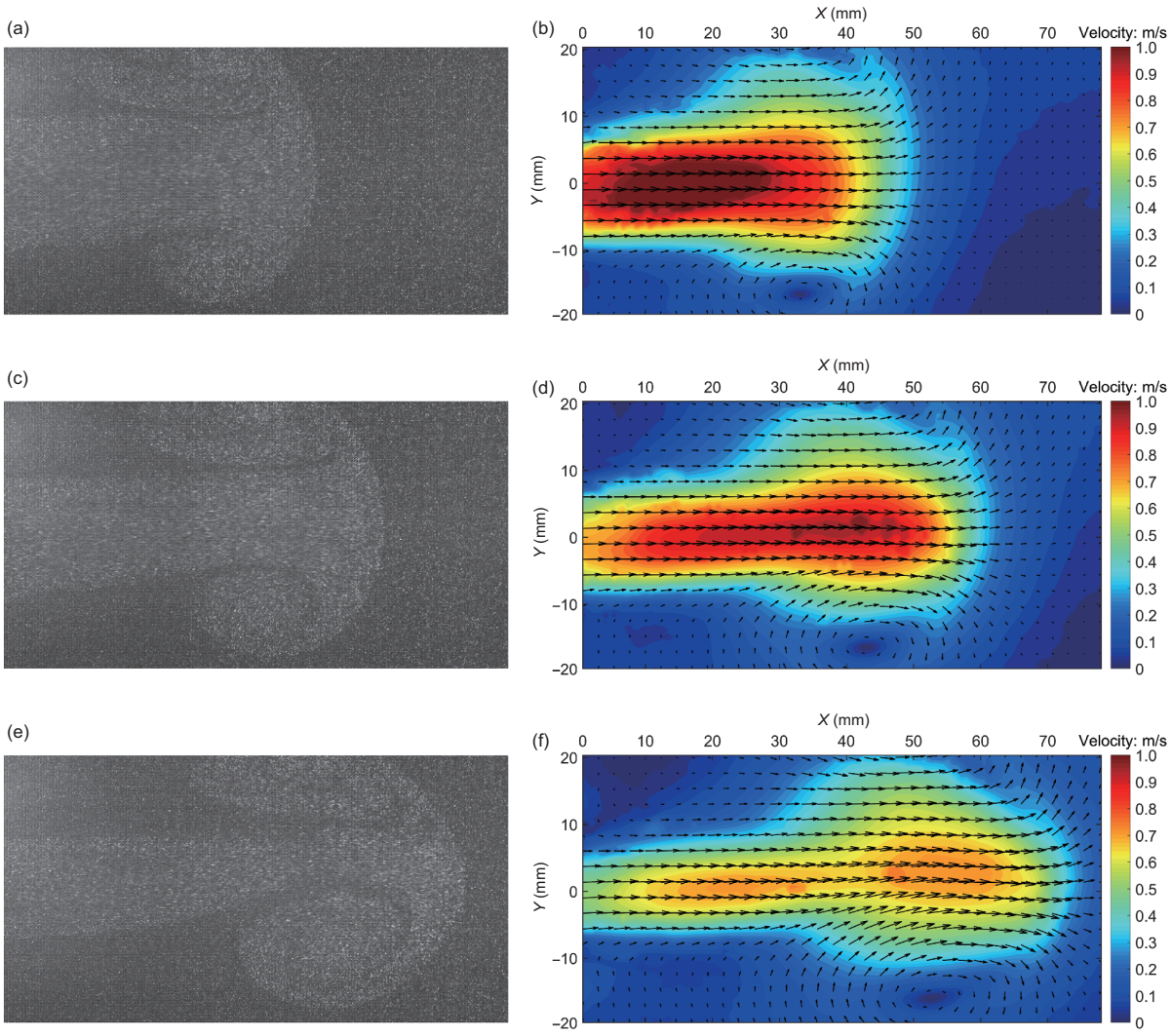

Figure 8 (Color online) The unsteady low speed jet flow field measured by the RTA-PIV method. (a), (c), (e) The PIV images of low speed jet flow at 0.3, 0.5 and 0.7 s, respectively; (b), (d), (f) the energy map and the vector map of low speed jet flow at 0.3, 0.5 and 0.7 s with the interval time 0.98, 1.07, and 1.24 ms, respectively.

CF-PIV32 will sometimes lose the ability to measuring the unsteady flow field. This indicates the necessity of adaptive interval time for the measurement of unsteady flow.

The energy map and the measured vector map can reflect the velocity field and reveal the mainstream and the circumfluence. With the proposed method CF-PIV32 with RTA, we can obtain the velocity field of the unsteady low speed jet flow field and structure of the velocity flow perfectly without the influence of the interval time initial set, which will cause the failure of the measurement with a fixed interval time.

5 Conclusions

In this study, an RTA-PIV method is proposed to accurately measure the instantaneous velocity field of an unsteady flow field. In the proposed closed-loop RTA-PIV method, a new correlation-filter-based PIV measurement algorithm is introduced to calculate the velocity field in real time. Then, a Kalman predictor model is established to predict the velocity of the next time instant and a suitable interval time can be determined. To adaptively adjust the interval time for capturing two particle images, a new high-speed frame-straddling vision system is developed for the proposed RTA-PIV method.

To fully analyze the performance of the RTA-PIV method, we conducted a series of numerical experiments on ground-truth image pairs and on real-world image sequences. The tests on particle images and experimental images have demonstrated the performance of the novel closed-loop real-time adaptive method. For the synthetic scalar sequence, the CF-PIV measurement algorithm can resolve image pairs better and offers a wider range of use, particularly for the measurement of unsteady flow fields. With the proposed RTA-

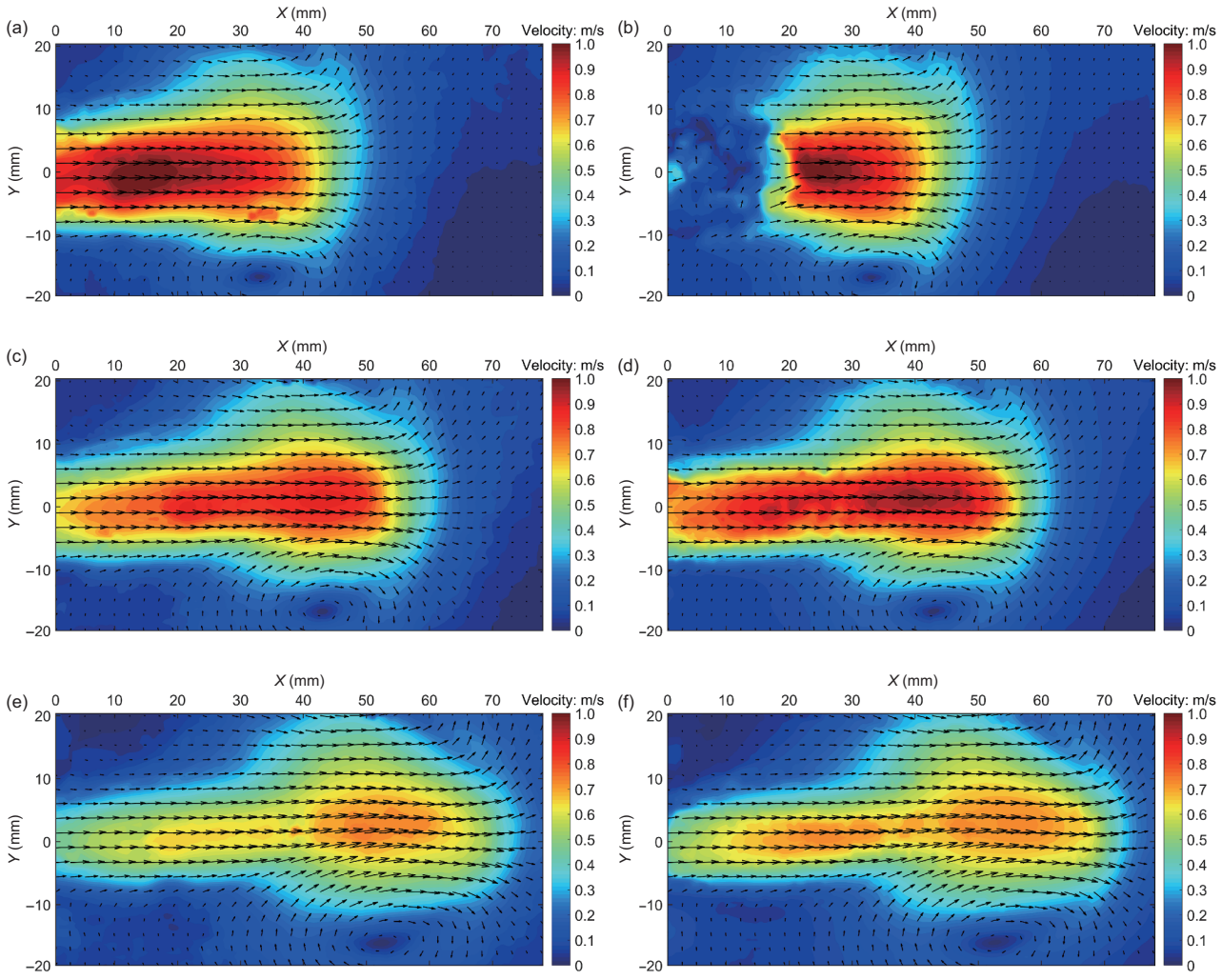

Figure 9 (Color online) The unsteady low speed jet flow field measured by CF-PIV32 with fixed interval time. (a), (c), (e) The energy map and the vector map of low speed jet flow at 0.3, 0.5 and 0.7 s with the fixed interval time 0.5 ms; (b), (d), (f) the energy map and the vector map of low speed jet flow at 0.3, 0.5, and 0.7 s with the fixed interval time 2 ms.

PIV method, we can obtain the velocity field and structure of the unsteady flow field perfectly without the influence of the initially set interval time. From the simulation and real experiments, one can know that the proposed RTA-PIV method can be used for the measurement of fluids with unsteady velocity fields, such as jet flow and laminar flows of micro-PIV, and especially time-varying flow.

This work was supported by the National Natural Science Foundation of China (Grant No. 51875228), the National Key R&D Program of China (Grant No. 2020YFA0405700), and the National Defense Science and Technology Innovation Special Zone Project (Grant No. 193-A14-202-01-23).

1 Schmidt B E, Sutton J A. Improvements in the accuracy of wavelet-based optical flow velocimetry (wOFV) using an efficient and physically based implementation of velocity regularization. Exp Fluids, 2020, 61: 32
2 Raffel M, Willert C E, Scarano F, et al. Particle Image Velocimetry: A Practical Guide. Berlin: Springer-Verlag, 2018
3 Peterson S D, Porfiri M, Rovardi A. A particle image velocimetry study of vibrating ionic polymer metal composites in aqueous environments. IEEE ASME Trans Mechatron, 2009, 14: 474–483
4 Lee Y, Yang H, Yin Z P. Outlier detection for particle image velocimetry data using a locally estimated noise variance. Meas Sci Technol, 2017, 28: 035301
5 Liu T, Salazar D M, Fagehi H, et al. Hybrid optical-flow-cross-correlation method for particle image velocimetry. J Fluids Eng, 2020, 142:
6 Wang H P, Wu P, Gao Q, et al. Spatial pyramidal cross correlation for particle image velocimetry. Sci China Tech Sci, 2018, 61: 867–878
7 Wang H, He G, Wang S. Globally optimized cross-correlation for particle image velocimetry. Exp Fluids, 2020, 61: 228
8 Pan C, Xue D, Xu Y, et al. Evaluating the accuracy performance of Lucas-Kanade algorithm in the circumstance of PIV application. Sci China-Phys Mech Astron, 2015, 58: 104704
9 Edwards M, Theunissen R. Adaptive incremental stippling for sample distribution in spatially adaptive PIV image analysis. Meas Sci Technol, 2019, 30: 065301
10 Theunissen R, Scarano F, Riethmuller M L. Spatially adaptive PIV interrogation based on data ensemble. Exp Fluids, 2010, 48: 875–887
11 Seong J H, Song M S, Nunez D, et al. Velocity refinement of PIV using

global optical flow. Exp Fluids, 2019, 60: 174
12 Zhou L, Shi W D, Cao W D, et al. CFD investigation and PIV validation of flow field in a compact return diffuser under strong part-load conditions. Sci China Tech Sci, 2015, 58: 405–414
13 Zhang L R, Xing J K, Wang J W, et al. Experimental study of the wake characteristics of a two-blade horizontal axis wind turbine by time-resolved PIV. Sci China Tech Sci, 2017, 60: 593–601
14 Kreizer M, Ratner D, Liberzon A. Real-time image processing for particle tracking velocimetry. Exp Fluids, 2010, 48: 105–110
15 Drazen D, Lichtsteiner P, Häfliger P, et al. Toward real-time particle tracking using an event-based dynamic vision sensor. Exp Fluids, 2011, 51: 1465–1469
16 Kobatake M, Aoyama T, Takaki T, et al. A real-time microscopic PIV system using frame straddling high-frame-rate vision. J Robot Mechatron, 2013, 25: 586–595
17 Akbaridoust F, Philip J, Hill D R A, et al. Simultaneous micro-PIV measurements and real-time control trapping in a cross-slot channel. Exp Fluids, 2018, 59: 183
18 Varon E, Aider J L, Eulalie Y, et al. Adaptive control of the dynamics of a fully turbulent bimodal wake using real-time PIV. Exp Fluids, 2019, 60: 124
19 Takehara K, Adrian R J, Etoh G T, et al. A Kalman tracker for super-resolution PIV. Exp Fluids, 2000, 29: S034–S041
20 Shi S, Chen D. Enhancing particle image tracking performance with a sequential Monte Carlo method: The bootstrap filter. Flow Measurement Instrum, 2011, 22: 190–200
21 Leroux R, Chatellier L, David L. Time-resolved flow reconstruction with indirect measurements using regression models and Kalman-filtered POD ROM. Exp Fluids, 2018, 59: 16
22 Henriques J F, Caseiro R, Martins P, et al. High-speed tracking with kernelized correlation filters. IEEE Trans Pattern Anal Mach Intell, 2015, 37: 583–596
23 Ouyang Z, Yang H, Huang Y, et al. A circulant-matrix-based hybrid optical flow method for PIV measurement with large displacement. Exp Fluids, 2021, 62: 233
24 Okamoto K, Nishio S, Saga T, et al. Standard images for particle-image velocimetry. Meas Sci Technol, 2000, 11: 685–691
25 Scarano F. Theory of non-isotropic spatial resolution in PIV. Exp Fluids, 2003, 35: 268–277
26 Wieneke B, Pfeiffer K. Adaptive PIV with variable interrogation window size and shape. In: Proceedings of the International Symposium on Applications of Laser Techniques to Fluid Mechanics. Lisbon, 2010
27 Ruhnau P, Kohlberger T, Schnörr C, et al. Variational optical flow estimation for particle image velocimetry. Exp Fluids, 2005, 38: 21–32
28 Corpetti T, Heitz D, Arroyo G, et al. Fluid experimental flow estimation based on an optical-flow scheme. Exp Fluids, 2006, 40: 80–97